



# Local valence analysis of 316L austenitic stainless steel produced by laser powder bed fusion

Kazuhisa Sato<sup>a,\*</sup>, Shunya Takagi<sup>a</sup>, Satoshi Ichikawa<sup>a</sup>, Takuya Ishimoto<sup>b,c,d</sup>, Takayoshi Nakano<sup>b,c</sup>

<sup>a</sup> Research Center for Ultra-High Voltage Electron Microscopy, Osaka University, 7-1 Mihogaoka, Ibaraki 567-0047, Japan

<sup>b</sup> Division of Materials and Manufacturing Science, Graduate School of Engineering, Osaka University, 2-1 Yamadaoka, Suita 565-0871, Japan

<sup>c</sup> Anisotropic Design & Additive Manufacturing Research Center, Osaka University, 2-1 Yamadaoka, Suita 565-0871, Japan

<sup>d</sup> Aluminium Research Center, University of Toyama, 3190, Gofuku, Toyama 930-8555, Japan

## ARTICLE INFO

### Keywords:

Additive manufacturing  
Laser powder bed fusion  
316L stainless steel  
Corrosion resistance  
Electron energy-loss spectroscopy

## ABSTRACT

Ultra-rapid cooling of laser powder bed fusion (LPBF) generates a cellular solidification microstructure with submicron-sized periodicity accompanied by non-negligible segregation. In 316L austenitic stainless steel, an important corrosion-resistant alloy, the effect of segregation, particularly variations in Cr concentration, on the corrosion resistance of the LPBF product is unknown. Local valence analysis of the LPBF-produced 316L by electron energy-loss spectroscopy revealed no obvious changes in the energy-loss near-edge structures of Cr and Fe measured within the solidification cellular microstructure, at the cell boundary, or at the melt-pool boundary. This result indicates that solidification segregation in the LPBF-produced 316L is unlikely to affect the corrosion resistance of the material.

## 1. Introduction

Laser powder bed fusion (LPBF) is a novel solidification process that achieves both high temperature gradient ( $G \sim 10^7$  K/m) and high solidification rate ( $R \sim 10^{-1}$  m/s). The most important feature of the LPBF is the ability to produce equiaxed grains, columnar grains, and even single crystals by controlling  $G$  and  $R$ , together with flexible shaping ability and high processing speed. Using this technique, 316L austenitic stainless steel (hereafter, LPBF 316L) has been widely studied so far [1–6]. Recent studies on the LPBF 316L using transmission electron microscopy (TEM) revealed that Cr and Mo concentrations increase at the cellular boundaries and decrease at the melt-pool boundary (MPB) due to solidification segregation [7,8]. It should be mentioned that the variation of Cr concentration may affect the corrosion resistance of the material. A comprehensive review has been reported on corrosion resistance of the LPBF 316L [9]; however, the relationship between solute segregation and chemical states has not been clarified so far. In this study, the effect of solidification segregation on the valence of Cr and Fe in the LPBF 316L was studied using electron energy-loss spectroscopy (EELS).

## 2. Materials and methods

The LPBF 316L was fabricated using an EOS M290 printer by scanning the laser beam bidirectionally along the X-axis [5,6]. The build direction is defined as the Z-axis and hence a parabolic MPB can be observed on the YZ-plane. A crystal grown under the low energy density condition was used in this study. Plan-view TEM specimens were prepared from a YZ-plane using a focused ion beam (FIB) instrument (Thermo Fisher Scientific Scios2). The structure and morphology of the prepared specimens were characterized using a 200 kV-TEM (JEOL ARM200F). Compositional analyses were performed by energy-dispersive x-ray spectroscopy (EDS) in the TEM. EELS was performed in scanning TEM (STEM) mode using a post-column energy filter (Gatan ContinuumK3).

## 3. Results and discussion

Fig. 1(a) shows a secondary electron image (SEI) of typical solidification cellular microstructures of a LPBF 316L (YZ-plane) after chemical etching. Crystallographic orientations are indicated below the figure, demonstrating the formation of crystallographic lamellar microstructure

\* Corresponding author.

E-mail address: [sato@uhvem.osaka-u.ac.jp](mailto:sato@uhvem.osaka-u.ac.jp) (K. Sato).

<https://doi.org/10.1016/j.matlet.2024.136978>

Received 28 May 2024; Received in revised form 4 July 2024; Accepted 6 July 2024

Available online 6 July 2024

0167-577X/© 2024 The Author(s). Published by Elsevier B.V. This is an open access article under the CC BY license (<http://creativecommons.org/licenses/by/4.0/>).

(CLM) [5,6]. Dislocation cell walls are seen as numerous vertical and inclined lines with bright contrast, which are mostly oriented in the  $\langle 100 \rangle$  direction. The cellular structures contribute to the strength of the material [5,6], and they are distinct from the intergranular continuous wetting layers despite the morphological similarities [10,11]. The same crystallographic orientations continue in the X-direction (depth direction of the image). The MPB is indicated by a double-arrowhead, which can be characterized by a gradually curved shape with a nearly flat bottom. Hereafter, TEM micrographs will be explained based on the crystallographic orientations and terminology shown in Fig. 1(a).

Fig. 1(b) shows a bright-field (BF) TEM image and the corresponding selected area electron diffraction (SAED) pattern of a specimen thinned by the FIB. A boundary indicated by the broken line is the lamellar boundary between the minor (left side) and the major (right side) layers. The SAED pattern was obtained from the major layer with  $[100]$  beam incidence. A boundary indicated by two arrowheads A-A' indicates a cell boundary inside the major layer. A high-resolution TEM (HRTEM) image obtained from the area enclosed by an open square is shown in the lower inset. Orthogonal  $(002)$  and  $(020)$  atomic planes are observed in the image. The cell boundary is the coherent interface, while the boundary can be identified since the slightly off-Bragg region is observed with brighter contrast (the crystal in the lower left area is slightly tilted in the  $[020]$  direction). Such a crystal tilt near the lamella boundary is presumed to be due to a local lattice correspondence between the major and the minor layers. No structural or chemical inhomogeneity was observed by atomic resolution imaging using either phase contrast (Fig. 1 (b)) or atomic number contrast (see Supplementary Fig. 1S).

Fig. 2(a)-(c) show the results of STEM-EDS elemental mapping obtained at a lamellar boundary between the minor and the major layers (indicated by a double-arrowhead). Small particles with dark contrast are inclusions composed of Mn-Si-O [7] (see Supplementary Fig. 2S). The EDS analysis revealed that Cr content increases ( $\sim 1$  wt%) at the lamellar boundary and at the cell boundaries (indicated by arrows) as shown in Fig. 2(b). Consequently, Fe content decreases at these boundaries (Fig. 2(c)). The small amount of compositional distribution at the lamellar or cell boundaries in the CLM is due to faint solute segregation during the rapid solidification by LPBF. Cell boundaries are often accompanied by entangled dislocations caused by thermal distortions (see Supplementary Fig. 3S).

STEM-EELS measurements were performed at the locations numbered 1 to 7 in Fig. 2(a). Fig. 2(d) shows core-loss spectra of Cr

including  $L_2$  and  $L_3$  edges. These two peaks, known as white lines, correspond to excitation of  $2p_{1/2}$  and  $2p_{3/2}$  core electrons to unoccupied  $3d$  states, respectively [12]. Therefore, the energy-loss near-edge structure (ELNES) reflects the density of unoccupied states. The intensity of the white lines is related to the total number of  $d$  holes of a transition metal, and hence it is sensitive to chemical state. For several chromium compounds, Daulton and Little [13] reported the correlation between intensity ratio  $L_3/L_2$  (white line ratio) and  $L_3$  peak energy with respect to Cr valence. They reported that  $L_3$  peak energy as well as the white line ratios are sensitive to the valence change such as due to oxidation. The measured spectra showed the same shape regardless of the solute segregation. Furthermore, energy shift (chemical shift) of the  $L_{23}$ -edges is negligible within the energy resolution of 1.0 eV in the present study. The white line ratio was evaluated as  $L_3/L_2 = 1.7 \pm 0.1$  for the Cr  $L_{23}$  edge. This value is slightly higher than that reported for metallic Cr ( $L_3/L_2 \sim 1.5$ ) [13,14]. No detectable oxide was observed by SAED, while there may be a contribution from a thin non-crystalline passivation film (hydrated chromium oxyhydroxide) formed on the surface of the TEM specimen.

Similarly, core-loss spectra for the Fe  $L_{23}$ -edges obtained from the points 1 to 7 entirely overlap with each other as shown in Fig. 2(e). The white line ratio was evaluated as  $L_3/L_2 = 3.1 \pm 0.1$  for the Fe  $L_{23}$ -edges. This value is consistent with that reported for pure Fe [14]. On the other hand, higher values of  $L_3/L_2$  over 4 have been reported for iron oxides [14]. The analyzed points 1, 4, and 5 are adjacent to inclusions as shown in Fig. 2(a), but there was no change in the ELNES of Cr and Fe. This result supports the recent report that nanoscale inclusions do not contribute to deterioration of the local corrosion resistance [3].

Fig. 3(a)-(c) show the results of STEM-EDS elemental mapping obtained at the MPB. The observed area is in a minor layer. A double-arrowhead in the BF-STEM image shown in Fig. 3(a) indicates a cell boundary. As can be seen in the EDS map (Fig. 3(b)), Cr content increases at the cell boundary ( $\sim 1$  wt%), similar to the results shown in Fig. 2(b). The dotted line indicates the location of MPB. In the LPBF process, crystal growth once stops at the MPB just before the solidification of the above layer starts. Consequently, Cr concentration slightly decreases by  $\sim 0.5$  wt% above the MPB (indicated by an arrow in Fig. 3 (b)) due to solidification segregation, which can be visualized by SEI after chemical etching (Fig. 1(a)).

STEM-EELS measurements were performed at the locations numbered 1 to 5 in Fig. 3(a). At the location 2, Cr concentration slightly

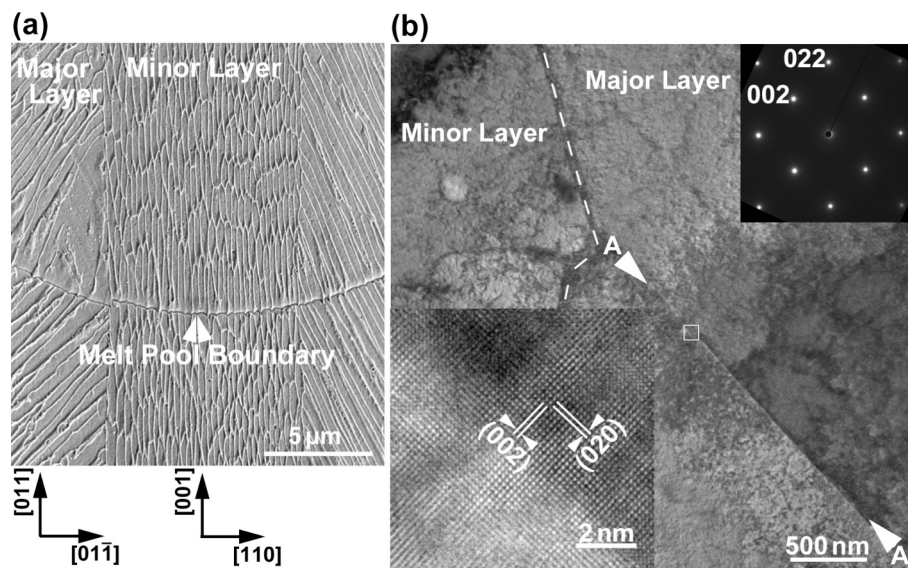


Fig. 1. (a) SEI of solidification cellular microstructures of the LPBF 316L. Crystallographic orientations are also shown. (b) BF-TEM image and the SAED pattern obtained from a region including a lamella boundary between the major and the minor layers. HRTEM image obtained from the area marked by a square is shown in the lower inset.

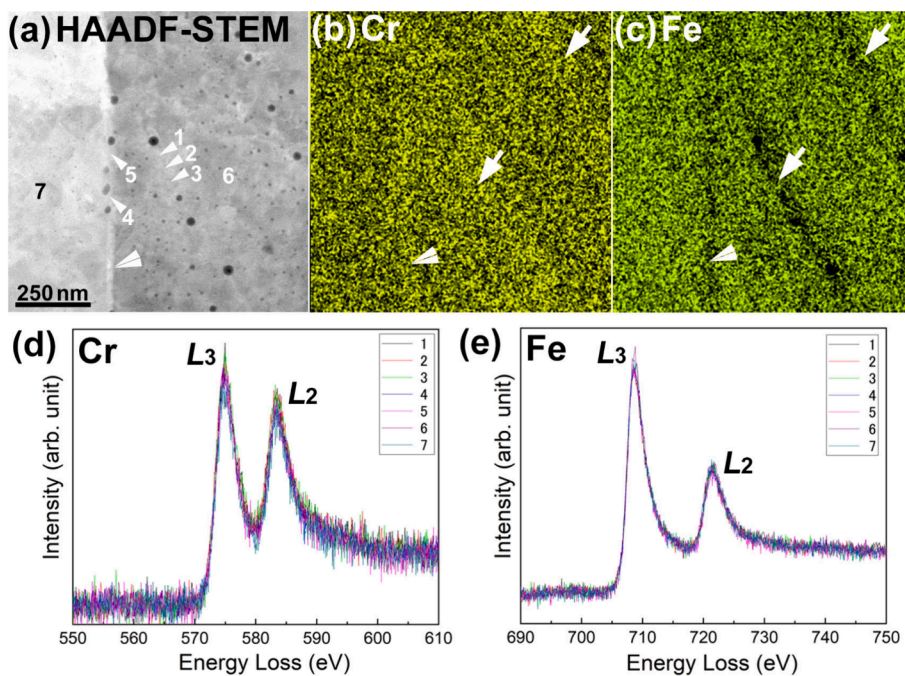


Fig. 2. (a) HAADF-STEM image, (b) EDS Cr map, (c) EDS Fe map, (d) EELS Cr  $L_{23}$ -edges, and (e) EELS Fe  $L_{23}$ -edges obtained near the cell boundary.

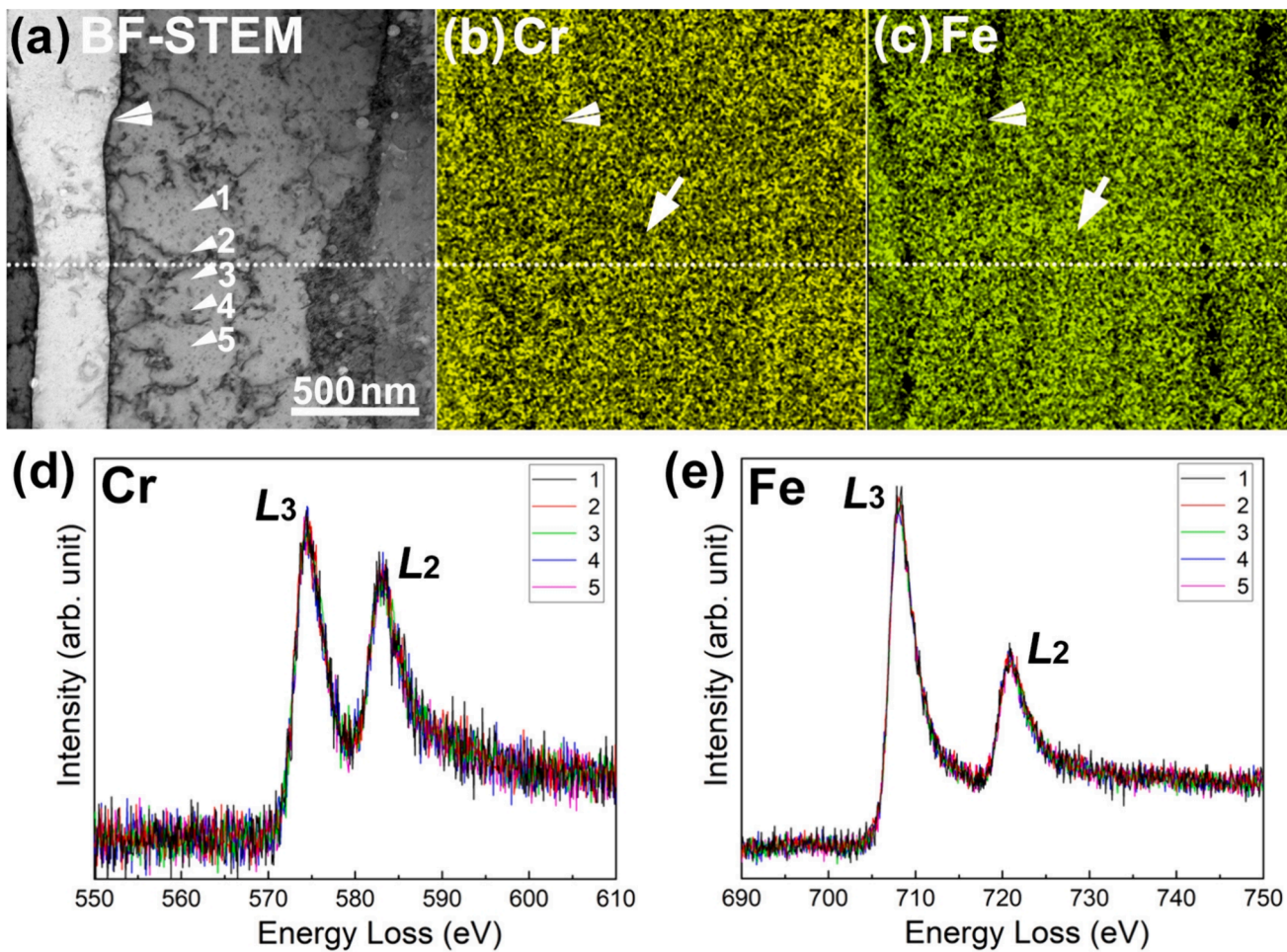


Fig. 3. (a) HAADF-STEM image, (b) EDS Cr map, (c) EDS Fe map, (d) EELS Cr  $L_{23}$ -edges, and (e) EELS Fe  $L_{23}$ -edges obtained near the melt-pool boundary (dotted line).

decreased as mentioned above. Fig. 3(d) shows core-loss spectra for the Cr  $L_{23}$ -edges. The measured spectra showed the same shape regardless of the solute segregation. The white line ratio was evaluated as  $L_3/L_2 = 1.6 \pm 0.1$  for the Cr  $L_{23}$ -edges, which is almost the same values obtained at the lamellar and the cell boundaries (Fig. 2(d)). Similarly, core-loss spectra for the Fe  $L_{23}$ -edges entirely overlap with each other as shown in Fig. 3(e). The white line ratio was evaluated as  $L_3/L_2 = 3.1 \pm 0.1$  for the Fe  $L_{23}$ -edges. These results clearly show that slight decrease in Cr concentration do not affect the corrosion resistance of the LPBF 316L.

#### 4. Conclusions

Local valence distribution of the LPBF 316L with CLM has been studied using (S)TEM with EDS and EELS. Comparing the energy loss spectra measured in the solidification cellular microstructure, at the cell boundary, and at the MPB, no obvious changes were observed in the  $L_{23}$ -edges of Cr and Fe. It was found that very small amount of solute segregation in the LPBF 316L produced via rapid quenching ( $\sim 10^6$  K/s) is unlikely to affect the oxidation states of the constituent elements, which partially contributes to the very high corrosion resistance of this material.

#### CRedit authorship contribution statement

**Kazuhiisa Sato:** Writing – original draft, Methodology, Investigation, Formal analysis, Conceptualization. **Shunya Takagi:** Investigation. **Satoshi Ichikawa:** Investigation. **Takuya Ishimoto:** Writing – review & editing. **Takayoshi Nakano:** Conceptualization.

#### Declaration of competing interest

The authors declare that they have no known competing financial

interests or personal relationships that could have appeared to influence the work reported in this paper.

#### Data availability

Data will be made available on request.

#### Acknowledgments

This study was supported by Grant-in-Aid for Transformative Research Area (A) (Grant No. 21H05196) from the JSPS and partly by JST-CREST (Nanomechanics) (Grant No. JPMJCR2194).

#### Appendix A. Supplementary data

Supplementary data to this article can be found online at <https://doi.org/10.1016/j.matlet.2024.136978>.

#### References

- [1] Y.M. Wang, et al., *Nat. Mater.* 17 (2018) 63–73.
- [2] M. Godec, et al., *Mater. Charact.* 160 (2020) 110074.
- [3] Y. Tsutsumi, et al., *Addit. Manuf.* 45 (2021) 102066.
- [4] T. Voisin, et al., *Acta Mater.* 203 (2021) 116476.
- [5] S.-H. Sun, et al., *Scripta Mater.* 159 (2019) 89–93.
- [6] T. Ishimoto, et al., *ISIJ Int.* 60 (2020) 1758–1764.
- [7] K. Sato, et al., *Materials* 16 (2023) 218.
- [8] F. Sun, et al., *Mat. Trans.* 64 (2023) 1143–1149.
- [9] V.B. Vukkum, R.K. Gupta, *Mater. Des.* 221 (2022) 110874.
- [10] B. Straumal, et al., *Coatings* 12 (2022) 343.
- [11] B. Straumal, et al., *Crystals* 13 (2023) 1538.
- [12] D.H. Pearson, et al., *Phys. Rev. B* 47 (1993) 8471–8478.
- [13] T.L. Daulton, B.J. Little, *Ultramicrosc.* 106 (2006) 561–573.
- [14] R.D. Leapman, et al., *Phys. Rev. B* 26 (1982) 614–635.